Engineering Studies into Vertical Lift Planetary Aerial Vehicles

Larry A. Young
Edwin W. Aiken
Army/NASA Rotorcraft Division
Ames Research Center
Moffett Field, CA
layoung@mail.arc.nasa.gov

M.R. Derby
J.L. Johnson
Aerospace Computing, Inc.
Mountain View, CA

J. Navarrete
J. Klem
San Jose State University

R. Demblewski
College of San Mateo

J. Andrews
Massachusetts Institute of Technology

R. Torres
New Mexico State University

Abstract

NASA Ames Research Center has been investigating various rotary-wing aeromechanics and proof-of-concept issues underlying the development of vertical lift aerial vehicles for planetary science missions. These engineering studies include: hover performance measurements of an isolated rotor in simulated Mars surface atmospheric conditions; radio-controlled coaxial helicopter flight tests supporting the investigation of Mars rotorcraft technologies; small-scale unducted- and ducted-fan hover tests that provide insight into possible VTOL aircraft for exploration of Titan; hybrid airship proof-of-concept testing that illustrates flight control and forward flight performance issues inherent in airships designed for flight in the atmosphere of Venus.

Introduction

Recent research has focused on the feasibility of developing vertical lift aerial vehicles that could aid in the exploration of various planetary bodies in our solar system. Specifically, the utility of vertical lift vehicles to support missions to Mars, Titan (a moon of Saturn), and Venus is being studied.

Achieving vertical flight for Mars, Titan, and Venus will not be easy to accomplish. Nonetheless, work to date has been promising (Mars: Refs. 1-16; Titan: Refs. 1-4 and 17-20; Venus: Refs. 1-4 and 21). Development of vertical lift planetary aerial vehicles will be a tremendous engineering undertaking – both in terms of technical challenge and scientific payoff.

This paper summarizes ongoing engineering studies conducted at NASA Ames Research Center into specific design issues related to vertical lift planetary aerial vehicles. The discussion will focus on the leading candidate vehicle concepts being studied at NASA Ames. It should not, however, be concluded that these concepts are the only viable aerial vehicles for planetary exploration, let alone the only vertical lift vehicle configurations that show promise. These are merely baseline concepts that allow the efficient definition, prioritization, and conduct of studies of key enabling technologies.

A baseline aerial vehicle concept for each of three planetary bodies will be briefly discussed. The paper then discusses ongoing work with regards to rotor and vehicle aeromechanics (ground) testing applicable to these planetary aerial vehicle concepts and proof-of-concept flight testing on terrestrial-analog, or surrogate, vehicles.

Atmospheric and physical properties for the three planetary bodies for which vertical lift aerial vehicles are being studied are given in Table 1.

Presented at the AHS International Meeting on Advanced Rotorcraft Technology and Life Saving Activities, Utsunomiya, Tochigi, Japan, November 11-13, 2002.

Table 1–Planetary Description (Ref. 22)

	Mean Radius (km)	Gravity (m/s^2)	Mean Surface Atmos. Temp. (^{o} K)	Mean Surface Atmos. Pressure (Pa)	Mean Surface Atmos. Density (kg/m^3)	Atmos. Gases
Mars	3390	3.71	214	636	$1.55x10^{-2}$	CO_2 95% N_2 2.7% Ar 1.6% O_2 0.1%
Titan	2575	1.354	94	149,526	5.55	N_2 65-98% Ar<25% CH_4 2-10%
Venus	6052	8.87	735.3	$9.21x10^6$	64.79	CO_2 96% N_2 3.5%

Mars Rotorcraft

Researchers at NASA Ames have been studying the design issues for Martian autonomous rotorcraft for the past several years. Several conceptual design studies of Martian autonomous rotorcraft – and other vertical lift planetary aerial vehicles -- have been conducted and reported by Ames and other researchers (Refs. 1-16).

The Martian atmosphere is 95% CO_2 with the remaining 5% comprised of N_2 and other trace gases (refer to Table 1). Mars' gravity is slightly greater than a third of Earth's. The atmosphere of Mars is extremely cold and thin (approximately 1% of Earth's sea-level atmospheric density). Further, a seasonal variation of approximately 20% of the planetary atmospheric mass occurs on Mars (a consequence of polar CO_2 condensation and sublimation). Given the thin, carbon-dioxide-based Martian atmosphere, developing a rotary-wing design is very challenging.

Concept Definition and Analysis

From an aeromechanics perspective, Mars rotorcraft will be very different from their terrestrial counterparts. Martian autonomous rotorcraft will have very large lifting-surfaces and will be required to have ultra-lightweight construction (Fig. 1). Further, rotors for flight in the atmosphere of Mars will operate with a unique combination of low Reynolds number and compressible flow aerodynamics.

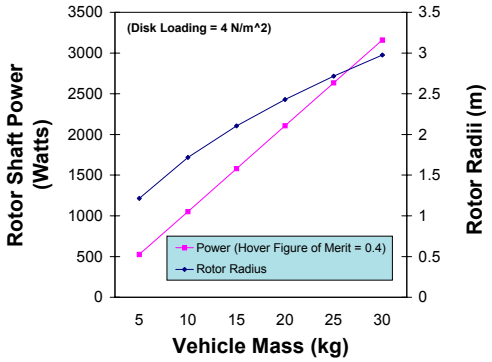

Fig. 1 – Sizing Trend for Mars Rotors

Conceptual design work to date has examined tiltrotor, quad-rotor, and coaxial helicopter configurations for Mars exploration. Both electric propulsion (batteries or fuel cells) and Akkerman hydrazine (mono-propellant) reciprocating engines have been examined for propulsion for these notional vehicles. Tiltrotor configurations would seem to be a longer-term candidate for Mars exploration as compared to the other two vehicle configurations as a consequence of the increased difficulties of the deploying a tiltrotor on the Mars surface (or mid-air descent). Electric propulsion appears to be a likely near-term candidate for Mars vertical lift vehicles because of comparative reliability, technology maturity, and environmental safety (hydrazine is a toxic substance that has to be carefully handled).

Currently, both coaxial and quad-rotor configurations – using electric propulsion and regenerative fuel-cell technology – continue to be seriously examined for NASA Mars Exploration and Mars Scout programs (Fig. 2).

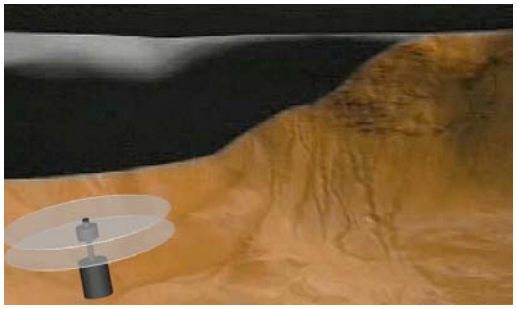

Fig. 2 – Mars Coaxial Helicopter

Additional supplemental discussion regarding the Mars rotorcraft mission architectures and challenges are given in Appendix C, along with similar discussion related to Titan and Venus vertical lift aerial vehicles. The focus of the paper now turns to specific engineering studies into Mars rotorcraft aeromechanics and terrestrial surrogate vehicle flight characteristics.

Rotor/Vehicle Aeromechanics Testing

Isolated rotor hover testing (Ref. 15) has been conducted in a large NASA Ames environmental chamber that can be reduced to atmospheric pressures and densities representative of the martian atmosphere. This requires the rotor airfoils to operate at very low Reynolds numbers and in compressible flow conditions.

A hover test stand and a baseline proof-of-concept rotor were fabricated and tested in the large environmental chamber. An advantage of rotorcraft, versus any other aerial vehicle proposed for Mars exploration, is the ability to conduct testing in existing ground-test facilities.

In conducting the experimental investigations, it was necessary to develop a 'baseline' proof-of-concept rotor. The baseline rotor is discussed in detail in Ref. 15. Figure 3 is a picture of the baseline proof-of-concept Mars rotor on its isolated rotor hover test stand. This four-bladed, 2.44 meter diameter rotor is approximately sized for a 10 kg coaxial Mars helicopter. The rotor geometric solidity is 0.191. The blade root cut-out is 40% of the rotor radius (so as to better simulate the blade folding, and perhaps telescoping, required for vehicle storage/transport). The blade outboard airfoil fairing is of constant chord (0.305 meter). This proof-of-concept rotor is a not an optimized design. The basic rotor construction approach, though, does emphasize the ultra-lightweight structures required for Mars rotorcraft. The baseline rotor was constructed of foam airfoil fairing and graphite epoxy composite spars and leading-edge caps. Details can be found in Ref. 15. Future generation Mars rotors will yield further improvements in weight and robustness, as well as improved dynamic tuning for forward-flight testing.

Fig. 3 – Baseline Proof-of-Concept Mars Rotor and Hover Test Stand

The baseline Mars proof-of-concept rotor uses an Eppler 387 airfoil for its constant chord outboard blade sections. (The inboard blade spar for the blade root cut-out is a circular graphite epoxy tube with a flat-plate chordwise stiffener.) The Eppler 387 is by no means an optimized airfoil for Mars rotor applications. A number of researchers are currently developing advanced airfoils for operating in the low-Reynolds number, compressible flow regime. These advanced airfoils will not only have potential application for Mars rotorcraft, but also to high-altitude long-endurance (HALE) aircraft and micro air vehicles. The Eppler 387 is, though, a well-documented low Reynolds airfoil and was chosen for that reason for the baseline Mars proof-of-concept rotor.

Isolated rotor performance results are shown in Figs. 4-7. Thrust versus power, thrust versus collective, and figure of merit curves for a variety of tip Mach and Reynolds numbers are presented. Details as to the methodology employed to estimate rotor shaft power is given in Appendix A. All data presented is shown with rotating bare shaft tares (but no hub tares) applied. The rotor performance data were acquired in air (versus carbon-dioxide) at a reduced atmospheric density of 1.24×10^{-2} kg/m^3 (approximately 80% of the "mean" Mars surface atmospheric density).

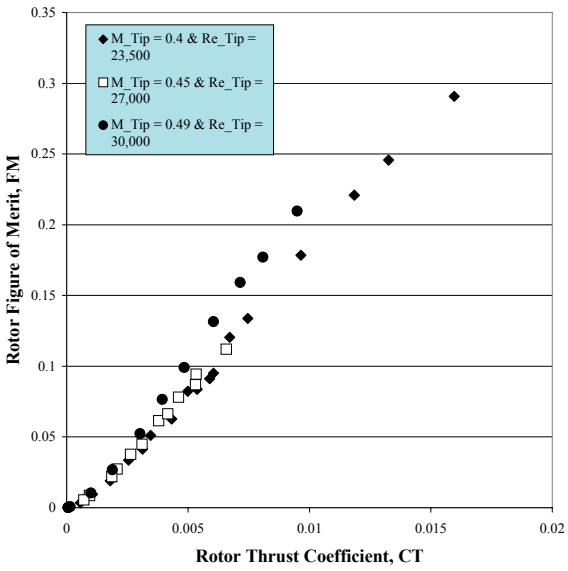

Fig. 4 – Mars Baseline Rotor Figure of Merit Curve (Bare Shaft Tare Applied; No Hub Tare)

Preliminary rotor thrust versus collective data for the Mars baseline rotor was presented in Ref. 15. Updated information, including rotor shaft power measurements and an improved viscosity equation to estimate tip Reynolds numbers, is included in Figs. 4-7. An initial attempt to predict the Mars baseline rotor hover performance characteristics was presented in Ref. 16. Significant disagreements are found between the experimental data and the

computational fluid dynamic (CFD) predictions. This is, in part, due to the fact that the design target tip Mach and Reynolds number conditions used in the CFD predictions (M_{Tip}=0.65 and Re_{Tip}=54,000) could not be matched in the baseline rotor hover test (the closest matching experimental conditions being M_{Tip}=0.49 and Re_{Tip}=30,000). This was primarily because the environmental chamber did not have a means to reduce the temperature of the chamber's working gas down to Mars-like levels, even though the target atmospheric densities could be achieved. Hopefully future work will reconcile the CFD and experimental results. The figure of merit results shown in Fig. 4 do not reveal the maximum figure of merit attainable for the Mars baseline rotor. This will also have to be established in future testing.

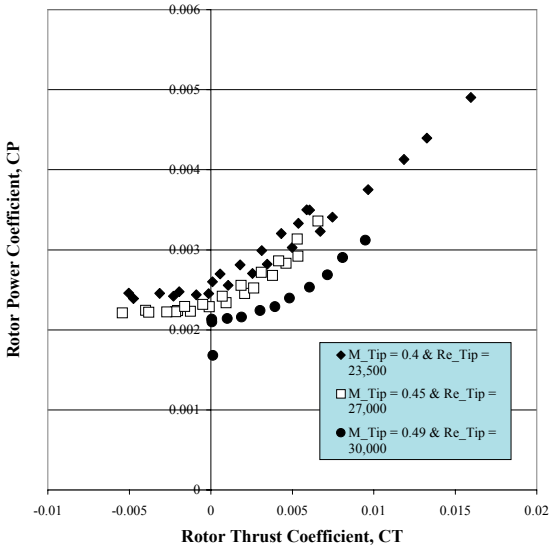

Fig. 5 – Thrust and Power Polar

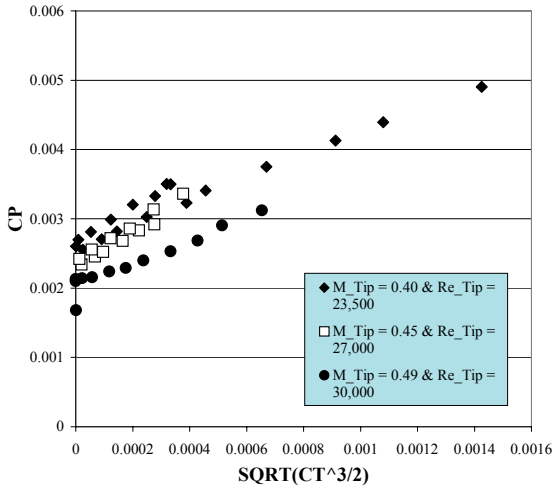

Fig. 6 – Measured Power Coefficient Trend with Respect to Ideal Power, $\sqrt{C_T^3/2}$

The effect of Reynolds number and/or tip Mach number can clearly be seen in the power polar data shown in Figs. 5-6. These particular combinations of Reynolds and Mach number seem to affect both the rotor mean profile drag coefficient, as well as potentially affecting the induced power constant. The Eppler 387 airfoil can exhibit highly nonlinear sectional lift/drag behavior at low Reynolds numbers, which is a result of the formation of leading-edge laminar separation bubbles (Ref. 23). The observed rotor tip Reynolds number aerodynamic sensitivity is not unduly surprising in this context. Unfortunately, insufficient rotor data exists to make a more definitive assessment of these Reynolds/Mach number effects. Future testing will be required.

Fairly high values of rotor profile power are seen in Fig. 5. The rotor profile power is significantly influenced by the sectional drag coefficient characteristics of the circular cylinder (with chordwise flat-plate stiffener) inboard blade spars.

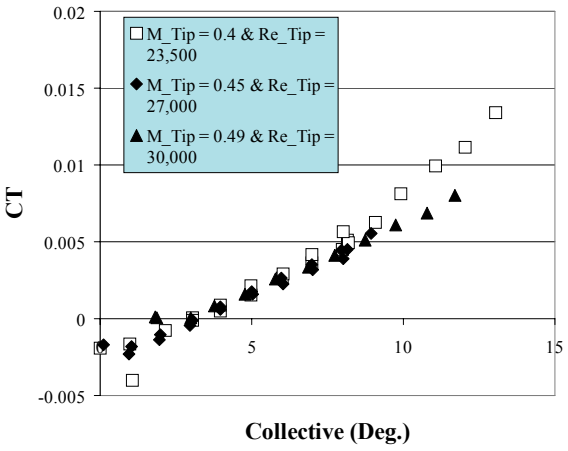

Fig. 7 -- Thrust Coefficient versus Collective

The rotor collective angles in Fig. 7 have been corrected to adjust for control system hysteresis that was observed in the Ref. 15 preliminary presentation of test results. Good agreement is now found to exist between the thrust versus collective curves after the applied corrections.

Terrestrial-Analog Testing

It is essential that not only are the aeromechanics of rotors and vehicles in simulated Martian environments are studied during the early stages of the concept development, but it is also necessary to perform terrestrial-analog demonstrations of the flight and mission characteristics of such vehicles.

A low-cost approach was taken in developing a coaxial helicopter flight demonstrator for terrestrial-analog studies (Fig. 8). Such vehicles are designated

as Terrestrial-Analog Mars Scouts (TAMS). A series of such vehicles is being developed. The TAMS vehicles are constructed primarily out of radio-controlled electric helicopter models.

(a)

(b)

Fig. 8 – Terrestrial-Analog (TAMS) Flight Demonstrator (a) on the ground and (b) in flight

The aerial survey potential for rotorcraft for Mars exploration is self-evident -- terrestrial rotorcraft have been used for this purpose from their earliest inception. But using rotorcraft as mobile 'sampling' devices to find, acquire, and return to lander-based in-situ analysis equipment will also be required for rotorcraft acting as 'Mars Scouts.' How rotorcraft might be adapted and used for soil/rock sampling missions is still being defined/assessed. As a part of that assessment a second TAMS vehicle has been developed that employs various types of robotic actuators and effectors to validate the utility of such devices in representative mission scenarios (Fig. 9).

Fig. 9 – Rock/Soil Sampling from a Robotic Helicopter

Titan Ducted-Fan VTOL Aircraft

Table 1 describes the general atmospheric characteristics of Titan, a moon of Saturn. Titan is the only moon in the Solar system that has a substantial atmosphere (Refs. 22 and 24). Several types of rotorcraft, or powered lift vehicles, could be developed for aerial exploration of Titan. Such vehicles will likely have electric propulsion driving their rotors or fans.

Concept Definition and Analysis

Ducted fan configurations such as tilt-nacelle aircraft are perhaps ideally suited for Titan (Fig. 10). Ducted fan aerial vehicles would inherently be more robust during take-off or landing in an unknown, potentially hazardous, environment as compared to conventional rotors. Figure 11 shows orthogonal views of a notional Titan vertical take-off and landing (VTOL) aerial vehicle.

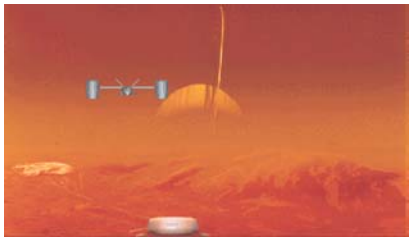

(a)

(b)

Fig. 10 -- A Titan Tilt-Nacelle VTOL: (a) take-off and (b) cruise (Background Image Courtesy of the ESA)

Figure 12 shows a first-order estimate of hover total shaft power for a notional Titan tilt-nacelle VTOL vehicle having two ducted fans that can pivot at the wing tips (similar in configuration to the Doak VZ-4). A shroud thrust fraction of 0.3 (i.e., 30% of the total thrust is provided by the duct/nacelle aerodynamics in hover) is used in the hover performance estimate. A figure of merit of 0.62 including the shroud thrust contribution is estimated for the Titan ducted fan vehicle. The hover performance and fan sizing estimates are for a disk loading of 600 N/m^2, a fan blade tip Mach number of 0.7, and a fan blade solidity of 0.25. A Titan VTOL's ducted fans will be very small and consume

very little power as a result of the high atmospheric density and low gravity field for Titan.

Fig. 11 – Orthogonal View of a Titan VTOL Concept

The mission concept being studied would employ a lander-based architecture where small ducted fan tilt-nacelle vertical take-off and landing aircraft could use the lander as a primary base site. The lander would service and support (including battery/fuel-cell recharging) the vertical lift aerial vehicles.

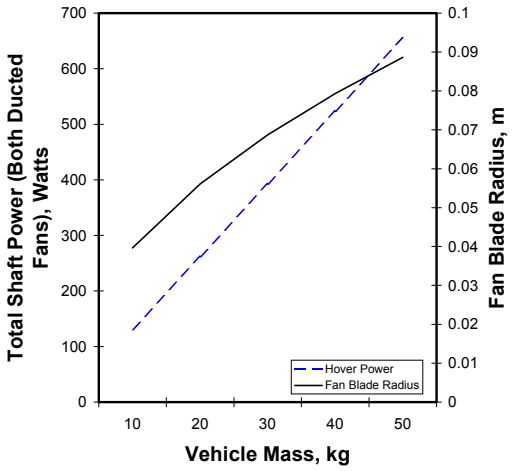

Fig. 12 – Ducted Fan Hover Performance for Titan Vehicle

Rotor/Vehicle Aeromechanics Testing

There has been a recent modest resurgence of research into ducted-fan VTOL vehicles at NASA Ames (for example, Ref. 25). The Titan VTOL research derives significant leveraging of complementary personal transport vertical lift vehicle and terrestrial UAV work ongoing within NASA Ames.

One the key assumptions of the Titan VTOL sizing studies done to date (Refs. 3, 4, and 17) is that substantial levels of lift augmentation can be generated by the fan ducts themselves. This thrust contribution is known as the shroud thrust fraction and can be much as 30 to 40% of the total vehicle lift in hover (Refs. 26-38). Hover testing of small-scale ducted fans/rotors was conducted in support of the Titan VTOL research (Fig. 13). The focus of the research was on ducted fans incorporating coaxial rotors which present several potential advantages, including propulsor compactness.

Fig. 13 – Coaxial Ducted Fan Hover Testing

Both unducted and ducted coaxial fan tests were conducted. The rotors used in the hover testing were derived from radio-controlled model helicopter hardware components. The rotors were two-bladed, had tapered planforms, used circular-arc flat-plate airfoils, and had a geometric solidity (per rotor) of 0.091. The rotors were also fixed-pitch, with very low bending/torsional stiffness. Rotor thrust was varied solely by speed control variations. Details of the data analysis methodology used in the hover testing are summarized in Appendix B.

To establish benchmark unducted fan performance, isolated rotor and unducted coaxial and tandem rotor performance measurements were made and compared to simple momentum theory predictions (Refs. 40-41). A simple approximate vortex theory is also derived and summarized in Appendix D. Figure 14a-b shows the comparison of induced power between theory and experimental results for coaxial rotors for a number of vertical separation distances. The coaxial rotor induced power ratio experimental results are shown both uncorrected and corrected for rotor load share imbalance (the thrust of one rotor is not exactly equal to that of the other) is shown in Fig 14a. The correction methodology for rotor load share imbalance is detailed in Appendix B. Only rotor load share corrections have been made in Fig. 14a-b. No load share corrections are made to the rest of the data presented in the paper. The experimental results are relatively constant with respect to the vertical rotor separation distance. This relatively flat profile of induced power ratio with respect to isolated rotor induced power has been observed by other researchers (Ref. 42). Figure 14b shows the experimental results to roughly fall within, or close

to, the induced power momentum theory limits of $P/P_I \rightarrow 1.41$ for very small vertical separation distances and $P/P_I \rightarrow 1.28$ for large h/R values (Ref. 40). Figure 14b also compares the corrected experimental results to predictions from a simple approximate vortex theory model. Predictions from this vortex theory model agree quite well with experimental results.

Figure 15 shows similar results for unducted tandem rotors. In general there is good agreement between theory (for small vertical separation distances) and experimental results except for the extreme points of the longitudinal rotor separation distances, s/R. The unducted tandem rotor momentum theory employed in Fig. 15 is from Ref. 40. Note that s/R = 0 is the uncorrected (with respect to rotor load share imbalance) coaxial rotor data. The unducted tandem rotor results will find application later in the paper in discussing elliptical/oval ducted fan configurations studied.

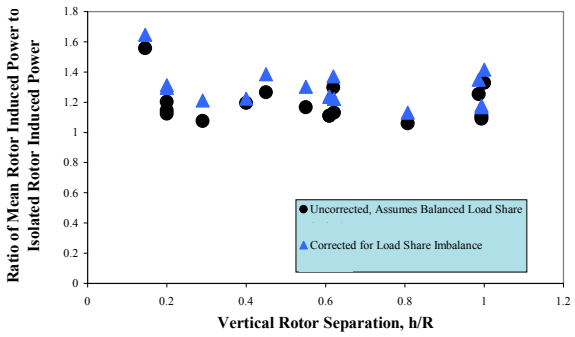

(a)

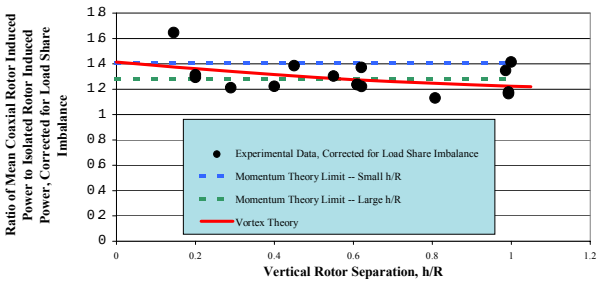

(b)

Fig. 14 – Unducted Coaxial Rotor (Induced Power) Performance: (a) Uncorrected and Corrected Experimental Results and (b) Momentum and Vortex Theory Predictions

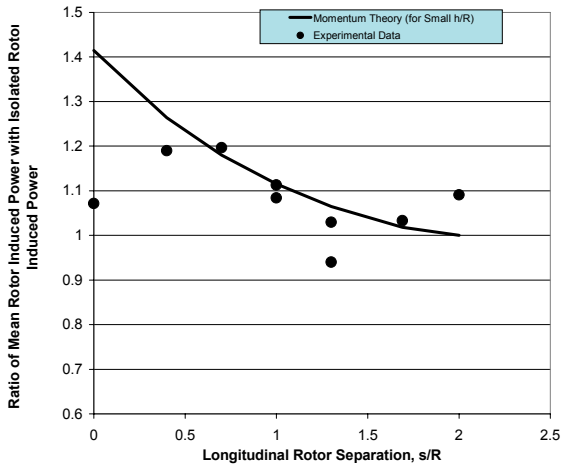

Fig. 15 – Unducted Tandem Rotor (Induced Power) Performance with Respect to an Isolated Rotor at Constant Thrust (h/R = 0.29)

The circular ducted fan hover testing was conducted with very simple ducts made of a thin layer of graphite epoxy composite. The duct depth was 12.4 cm; the diameter of duct inlet, including the lip edge, was 40 cm; the radii of the curved portion of the duct lip was 3.175 cm (the front face of the duct lip was flat); the duct inner diameter was 30 cm. The tip clearance between the rotors and duct inner lining was 3.5% of the rotor radii – a fairly large clearance for ducted fans. The rotors were always centered in the duct when parametrically varying the rotor-to-rotor vertical spacing – i.e. the rotor hubs were always spaced equidistant from a point halfway along the duct axis.

Despite a simple duct design and construction (really only feasible for the type of low Reynolds number testing conducted), exceptionally good results were achieved for the circular ducted fan configurations. Figure 16 shows that the circular ducted fans tested had shroud thrust fractions ranging from 1.1 to 1.4 depending on the rotor to rotor vertical spacing in the duct. This result compares nicely with similar results in the literature for VTOL ducted fan vehicles. Nonetheless, these are not optimized ducted-fan configurations. For example, tuft flow visualization reveals that there is separated flow along the interior of the duct wall between the two rotors for the h/R =0.45 configuration – and so there is plenty of opportunity for improvements. Further, the simple ducts tested are acceptable for hover but need to be improved for transition and cruise forward flight. (A shroud thrust fraction of 1.3 was used to generate the Fig. 12 Titan VTOL performance estimates.)

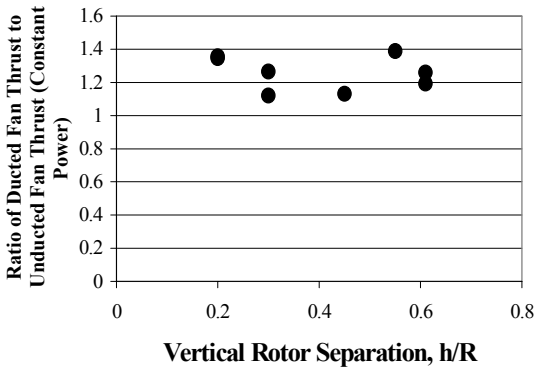

Fig. 16 – Circular Ducted Fan Lift/Thrust Augmentation (Constant Power)

Figure 17a-b compares circular ducted fan performance against isolated rotor performance. Circular ducted fan lift/thrust augmentation has two components. First, there is in general an increase in mean thrust, $T_{DF}/T_I > 1$, (where T_{DF} is total thrust for the ducted fan divided by a factor two) due to suction pressure across the inlet lip of the duct as flow is entrained into it. Second, there is a power reduction, $P_{DF}/P_I < 1$, (where P_{DF} is total power for the ducted fan divided by a factor two) due to beneficial interaction of the rotors with the duct walls.

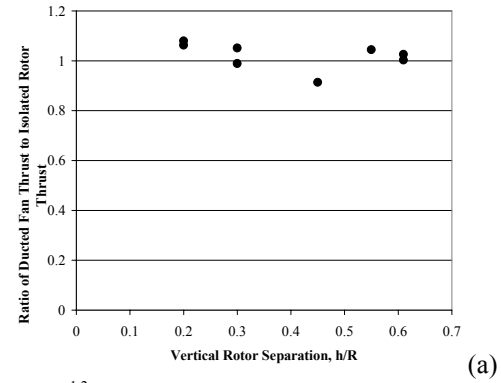

(a)

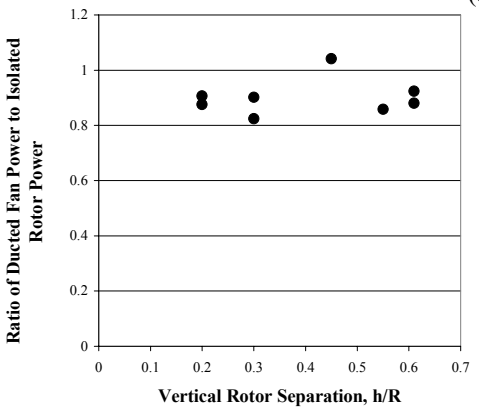

(b)

Fig. 17 – Circular Ducted Fan Performance (a) thrust ratio at constant speed/collective and (b) power ratio at constant thrust

Work has also been performed on the aerodynamic performance characteristics of an "elliptical duct-fan" -- or more correctly an oval ducted fan -- vehicle concept (Fig. 18). A coaxial ducted-fan vehicle can be thought of as a special case, s/R=0, of the more general "elliptical duct" vehicle configuration (Fig. 19a-b). One of the more difficult challenges of developing a VTOL aircraft is defining a simple, but extremely robust, flight control system for such vertical lift vehicles. Quad-rotor, or propulsor, concepts provide exceptional flight control characteristics but suffer from complexity and aerodynamic performance issues, whether it is in hover, transition, or cruise forward-flight. The "elliptical duct" VTOL concept offers the promise of simple speed control of four rotors/fans for aircraft roll and pitch trim, while retaining relatively good aerodynamic performance characteristics. If validated, the "elliptical duct" VTOL could be applicable to both micro-rotorcraft and planetary aerial vehicle applications. The work described in this paper is the first initial steps in evaluating the merits of this vertical lift vehicle concept.

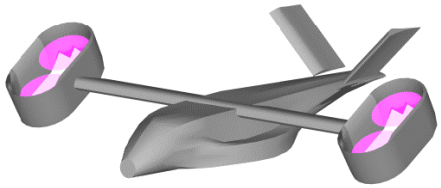

Fig 18 – Elliptical Ducted-Fan Vehicle Configuration

A significant effort was expended to examine the key parametric influences of rotor/fan longitudinal and vertical separation distances (s/R and h/R) on rotor performance for both the unducted and ducted rotors/fans (Figs. 20a-b and 22). Details of the experimental apparatus and the performance data reduction are provided in Appendix B.

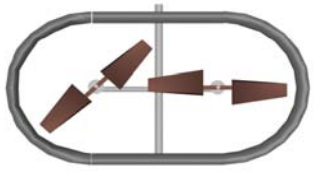

(a)

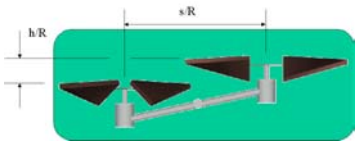

(b)

Fig. 19 -- Elliptical/Oval Duct Fan Layout– (a) duct interior and (b) cross-sectional view

With respect to Fig. 20a-b, the behavior of the unducted fan "tandem" rotor data is consistent in general with expectations: a net mean thrust loss is

seen for tandem rotors compared to isolated rotors, and, further, mean rotor power increases with respect to isolated rotor levels as the (both vertical and longitudinal) separation distance is reduced. There are some surprising observed behaviors as s/R approaches zero, or is greater than 1.3. Note again that s/R=0 data are the coaxial rotor cases.

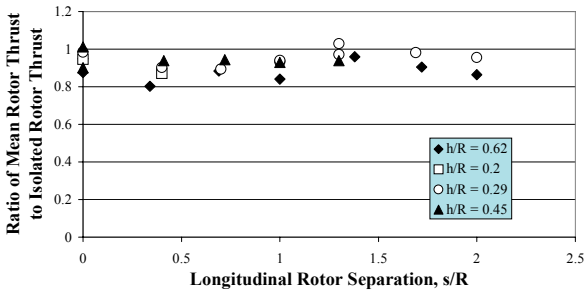

(a)

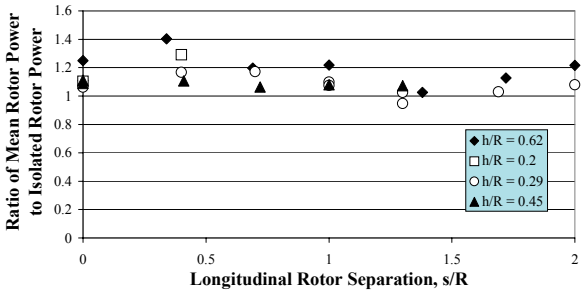

(b)

Fig. 20 – Unducted "Tandem" Fan Performance (a) thrust at constant speed/collective and (b) power at constant thrust

Elliptical (oval) ducted fan testing was conducted for a similar parametric set of vertical and longitudinal rotor separation distances as was performed for the unducted "tandem" rotor configurations. Figure 21 shows a picture of the experimental installation of a elliptical ducted fan on the same basic test stand/apparatus as the isolated rotor, unducted coaxial/tandem rotors, and circular ducted fans were tested on.

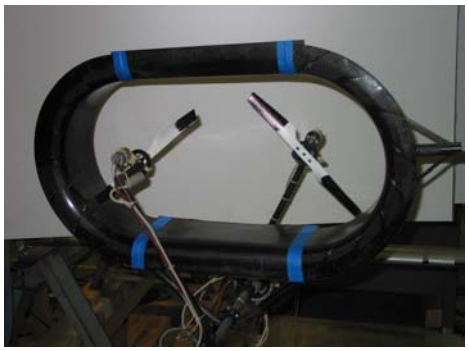

Fig. 21 – Elliptical Ducted Fan Test Installation

Figure 22 shows the effect on ducted fan lift augmentation as a function of longitudinal rotor to rotor separation, s/R, for two different vertical separation settings, h/R = 0.3 and h/R = 0.62. Unlike initially expected, there is no reduction in lift/thrust augmentation with increasing s/R. In all cases studied, good duct lift/thrust augmentation (over the unducted configurations) is preserved. This result bodes well for the viability of the elliptical ducted-fan concept. The inherent rotor-to-rotor separation will enable the use of rotor speed control for vehicle pitch and roll control, while at the same time not forcing a substantial performance penalty.

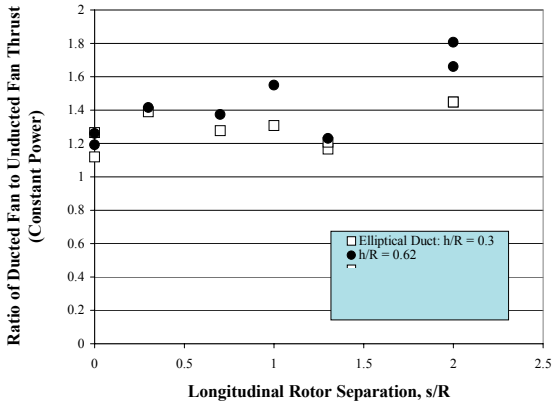

Fig. 22 – 'Elliptical' Ducted-Fan Performance (constant power)

Given prior work indicated in Refs. 27 and 40, a simple momentum theory expression can be derived for the ratio of ducted fan induced power to unducted fan induced power for oval ducted fans (refer to Appendix D). This expression includes the introduction of a duct efficiency factor, ε, ($0 \le \varepsilon \le 1$). Ideal duct performance predicted when ε=1. When ε=0 the P_{DF}/P_{UDF} (induced power)=1 for all s/R values.

Figure 23 compares the above momentum theory expression with experimental data for the elliptical (oval) ducted fan hover testing. Predictions are made for both the ideal case (ε=1) and an assumed duct efficiency of ε=0.35. There is very good agreement between the simple momentum theory for oval ducted fans and the test results.

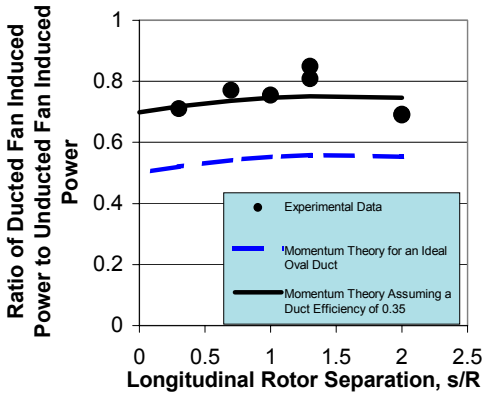

Fig. 23 – Elliptical (Oval) Ducted Fan Induced Power at Constant Thrust (h/R=0.29)

Terrestrial-Analog Testing

A series of model-scale terrestrial-analog flight vehicle tests continue to be conducted at NASA Ames exploring the unique flight characteristics of unducted-fan and ducted-fan vertical lift vehicles (for example, Fig. 24). Despite the large body of work to be found in the literature regarding the terrestrial applications of ducted-fan VTOL vehicles, a considerable amount of work remains to be performed to assess the operational characteristics for planetary science applications.

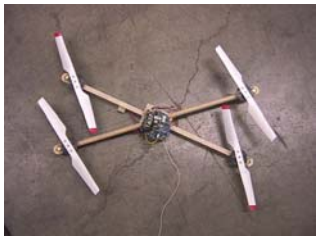

Fig. 24 – Variable Separation Study Platform (VSSP)

The Army/NASA Rotorcraft Division at Ames Research Center is currently collaborating with the NASA Minority University Education Program at NASA Headquarters to sponsor and conduct a student design competition for Titan VTOL concepts and missions. This competition will be held in the 2003 academic year (Ref. 39). This NASA Titan VTOL design competition will complement the 2000 AHS International, NASA, and Sikorsky Aircraft student design competition for a Martian autonomous rotorcraft (Refs. 10-14). It is anticipated that the Titan VTOL design competition will not only be an excellent educational outreach opportunity, but, additionally, might ultimately contribute to NASA's Outer Planet/New Horizons programs.

Venus Hybrid Airship

Of the three planetary bodies besides Earth where it theoretically might be feasible to design and fly vertical lift aerial vehicles, Venus will likely pose the greatest challenge. The atmosphere of Venus is extremely hot and dense near its surface (refer to Table 1).

Concept Definition and Analysis

The extremely high atmospheric densities near Venus' surface (plus the near-Earth-magnitude of its gravitational field) would suggest that a buoyant, or semi-buoyant, vehicle might represent the most practical design for exploration of Venus (Fig. 25). The airframe of a Venusian hybrid-airship would be a rigid hull, which would have to be able to sustain substantial pressure differentials across the hull surface.

Venus' high surface temperatures also pose tremendous challenges for aerial vehicle design. Though active and passive technologies exist for thermal management of planetary science hardware, extended operation of such hardware near Venus' surface is currently problematic with today's technology. This will, therefore, mean that the lift (and power) required for take-off and landing will need to be kept to an absolute minimum (thus necessitating buoyancy fractions greater than 75%).

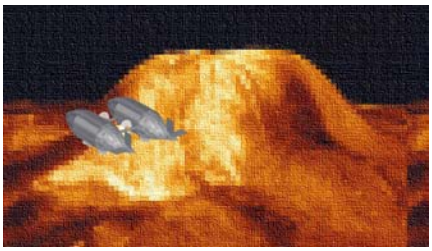

Fig. 25 -- A Notional Venusian Hybrid Airship with Twin Hulls and Tandem Tilting Propellers and Wings

Figure 26 shows first-order estimates of a notional Venus hybrid-airship's hull size. The results shown in this figure assumes a hybrid-airship buoyancy fraction of 0.9 and a propulsion energy-source (batteries, fuel cells, etc.) weight fraction of 25%. Helium is assumed as the hybrid-airship lifting gas. A thin skin of titanium alloy is assumed for the hull. Hull skin thickness using titanium alloys ranges from 0.5 to 1mm thick for vehicle mass from 10 to 50 kg.

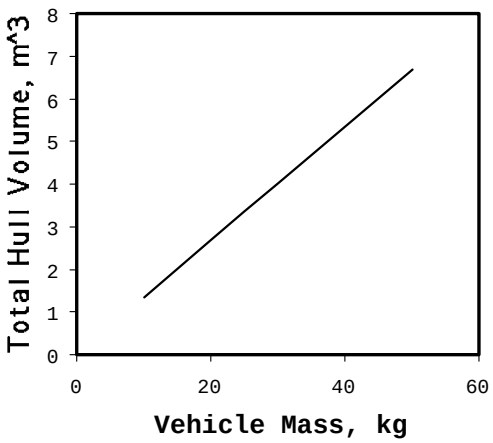

Fig. 26 – Hull(s) Size Estimate

Figure 27 is an orthogonal view of the notional Venus hybrid airship concept being studied at NASA Ames.

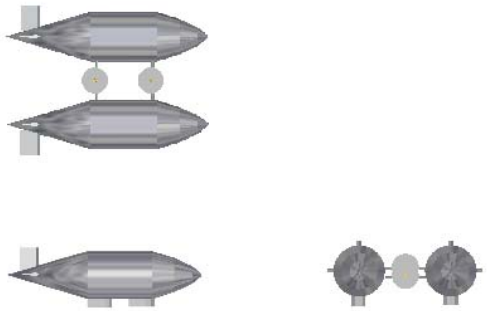

Fig. 27 – Notional Venus Hybrid-Airship Orthogonal View

Figure 28 shows a first-order estimate of the hover performance and sizing of a tandem propeller combination (sandwiched between twin airship hulls) that could be used to take-off and land from Venus' surface. The performance and sizing estimates shown in the figure assume the airship buoyancy fraction of 0.9 (therefore, the two propellers have to lift only 10% of vehicle weight in hover), a tip Mach number of 0.1, a 200 N/m^2 disk loading, and a solidity of 0.4 for the propellers. A 2% download for the tiltwings supporting the rotors was used in the hover performance estimate. A figure of merit of 0.48 (including the effect of download) was estimated for the hybrid airship configuration.

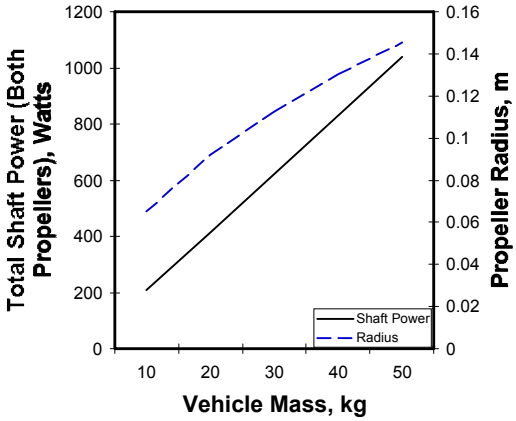

Fig 28 – Hybrid-Airship Propeller Hover Performance and Sizing Estimates

Rotor/Vehicle Aeromechanics

A twin-hull configuration for hybrid airships presents unique aerodynamic challenges for aerodynamic static stability characteristics due to interactional aerodynamic influences of ellipsoidal bluff bodies in close proximity. Low speed wind tunnel testing is planned to assess these interactional aerodynamic phenomena for ellipsoidal bodies in close side-by-side proximity (Fig. 29).

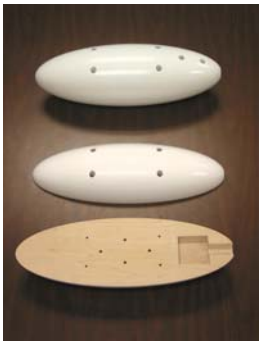
(a)

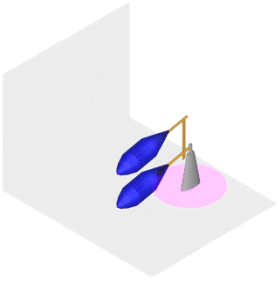
(b)

Fig. 29 – Wind Tunnel Testing for Ellipsoidal Bluff Body Interactional Aerodynamics (a) test models and (b) test installation

Terrestrial-Analog Testing

Relying again upon readily available radio-controlled model components, a simple proof-of-concept model was built to demonstrate key attributes of the twin hull Venus hybrid airship concept.

The initial proof-of-concept vehicle relied on four rotors to provide lift, forward propulsion, and yaw control. The spar separating both airship hulls was structural only and did not provide any lift during forward flight. Despite the design compromises for the proof-of-concept terrestrial surrogate vehicle, the basic conceptual feasibility of the twin-hull hybrid airship was established. Stable but maneuverable flight was demonstrated in closed laboratory environment (Fig. 30a-b). Take-off and landings and precision handling were demonstrated.

(a)

(b)

Fig. 30 – Proof-of-Concept Surrogate Vehicle (a) front view, in flight in the laboratory, and (b) side view

Future Plans

The near-term focus of the vertical lift planetary aerial vehicle research will begin to be directed towards two efforts: the Mars Smart Rotorcraft Field Agent (SRFA) project which is in response to the NASA Astrobiology Science and Technology for Exploring Planets Announcement of Opportunity (Ref. 43), and support of a NASA-sponsored Minority University (Ref. 39) student design competition on Titan VTOL aircraft. The Mars SRFA project will equally focus on Mars rotorcraft aeromechanics issues, as well as demonstrator development and terrestrial surrogate vehicle field trials.

The SRFA terrestrial surrogate vehicles will be tested during a field campaign at Haughton Crater, Devon Island, Canada (Fig. 31). The field campaign will continue ongoing astrobiology research at Haughton and will demonstrate a systems level capability to carry out such research on Mars. The rotorcraft will be instrumented with imaging instrumentation for aerial reconnaissance of multiple sites including ones that are otherwise inaccessible. The rotorcraft will be equipped with a panoramic camera for surface characterization and will have a mechanism on each landing leg to automatically acquire a soil sample. A special all terrain vehicle (ATV) will include a science platform equipped with a close-up camera and Raman spectrometer.

Fig. 31 – Mars-Analog Site Field Demonstrations of Surrogate Vehicles (Background Image Courtesy of the SETI Institute)

The SRFA system (which includes the ATV) will include data analysis software to discriminate autonomously between different rock-forming minerals and to identify certain classes of micro-organisms. The capability in question will be an augmentation of the on-going development at NASA Ames of a "Geology Field Assistant". This software agent combines information about the physical characteristics of rocks (e.g. texture, grain size, color) with diagnostic spectral characteristics to identify the minerals that compose the rock in question. The spectral characteristics of micro-organisms provide a similar means of detecting such organisms in the soils at sites of interest in the Haughton complex.

Concluding Remarks

The development of vertical lift planetary aerial vehicles could potentially represent an important new capability in the exploration of our solar system. Planetary aerial vehicles could aid in such momentous scientific endeavors as the ‘search for water’ and the ‘hunt for life’ on Mars, the investigation of fundamental pre-biotic organic

chemistry processes on Titan, and the understanding of geologic and atmospheric evolutionary processes of our 'sister' planet, Venus. Vertical flight will provide the essential component of three-dimensional mobility required for these important scientific investigations.

Engineering studies continue to be pursued at NASA Ames Research Center as to vertical lift planetary aerial vehicles. Vehicle concepts and associated experimental work investigating their feasibility is being conducted. Several experimental results are presented for Mars rotors under simulated Mars-like conditions, unducted and ducted fan.rotor results with potential application to a Titan VTOL aircraft. And terrestrial surrogate vehicle, proof-of-concept, flight testing for potential Venus hybrid airships.

Over five hundred years ago, the vision of vertical flight was first conceived by Leonardo de Vinci. Approximately one hundred and fifty years ago, the first steps toward automated computation and analysis were taken by Charles Babbage. Nearly one hundred years ago, first flight with a heavier than air powered aircraft was ultimately achieved by Orville and Wilbur Wright. Now, in the twenty-first century, a call is being sounded to a new generation from whom future Martian aviators and planetary aerial vehicle designers will be drawn. The golden age of flight is not in the past, but in the future. First flight will be achieved yet again – this time against alien skies.

Acknowledgments

The authors would like to acknowledge the contributions in support of this paper of: Garrett Kramer, Jim Phoreman, and Dr. Ron Greeley of Arizona State University; and Dr. Farid Haddad and Dr. Johanne Van Aken of the Army/NASA Rotorcraft Division. Further, the continued collaboration of Dr. Geoffrey Briggs of the NASA Ames Center for Mars Exploration and Dr. Virginia Gulick, of the SETI Institute in the area of vertical planetary aerial vehicles is gratefully acknowledged.

References

1. Young, L.A., et al, "Design Opportunities and Challenges in the Development of Vertical Lift Planetary Aerial Vehicles," American Helicopter Society (AHS) Vertical Lift Aircraft Design Conference, San Francisco, CA, January 2000.

2. Aiken, E.W., Ormiston, R.A., and Young, L.A., "Future Directions in Rotorcraft Technology at Ames Research Center," 56th Annual Forum of the American Helicopter Society, International, Virginia Beach, VA, May 2-4, 2000.

3. Young, L.A., "Vertical Lift -- Not Just For Terrestrial Flight," AHS/AIAA/SAE/RaeS International Powered Lift Conference, Arlington, VA, October 30-November 1, 2000.

4. Young, L.A. and Aiken, E.W., "Vertical Lift Planetary Aerial Vehicles: Three Planetary Bodies and Four Conceptual Design Cases," 27th European Rotorcraft Forum, Moscow, Russia, September 11-14, 2001.

5. Savu, G. and Trifu, O. "Photovoltaic Rotorcraft for Mars Missions," AIAA-95-2644, 1995.

6. Gundlach, J.F., "Unmanned Solar-Powered Hybrid Airships for Mars Exploration," AIAA 99-0896, 37th AIAA Aerospace Sciences Meeting and Exhibit, Reno, NV, January 11-14, 1999.

7. Kroo, I., "Whirlybugs," New Scientist, June 5, 1999.

8. Young, L.A., et al, "Use of Vertical Lift Planetary Aerial Vehicles for the Exploration of Mars," *Concepts and Approaches for Mars Exploration*, Lunar and Planetary Institute (LPI) Report # 1062, Houston, TX, July 18-20, 2000.

9. Young, L.A., Aiken, E.W., Gulick, V., Mancinelli, R., and Briggs, G.A., "Rotorcraft as Mars Scouts," IEEE Aerospace Conference, Big Sky, MT, March 9-16, 2002.

10. Healey, A. "Mars Explorer," *Helicopter World*, Shephard Publishing Group, London, England, December 1999.

11. Thompson, B., "Full Throttle to Mars," *Rotor & Wing*, Phillips Business Information, LLC, Potomac, MD, March 2001.

12. University of Maryland Year 2000 AHS Student Design Competition Proposal on the "Development of Rotary-Wing Technologies for Use in Mars Exploration" (http://www.enae.umd.edu/AGRC/Design00/MARV.html).

13. Georgia Institute of Technology Year 2000 AHS Student Design Competition Proposal on the "Development of Rotary-Wing Technologies for Use in Mars Exploration" (http://www.ae.gatech.edu/research/controls/projects/mars/reports/index.html).

14. Datta, A., et al, "Design of the Martian Autonomous Rotary-wing Vehicle," AHS

Specialist's Meeting on Aerodynamics, Acoustics, and Test and Evaluation, San Francisco, CA, January 23-25, 2002.

15. Young, L.A., Aiken, E.W., Derby, M., Demblewski, R., and Navarrete, J., "Experimental Investigation and Demonstration of Rotary-Wing Technologies for Flight in the Atmosphere of Mars," 58th Annual Forum of the AHS, International, Montreal, Canada, June 11-13, 2002.

16. Corfeld, K., Strawn, R., and Long, L., "Computations on a Prototype Martian Rotorcraft," AIAA 20th Applied Aerodynamics Conference, St Louis, MO, June 2002..

17. Young, L.A., "Exploration of Titan Using Vertical Lift Aerial Vehicles," *Forum on Innovative Approaches to Outer Planetary Exploration 2001-2020*, Lunar and Planetary Institute (LPI) Report # 1084, Houston, TX, February 21-22, 2001.

18. Lorenz, R.D., "Post-Cassini Exploration of Titan: Science Rationale and Mission Concepts," Journal of the British Interplanetary Society (JBIS), Vol. 53, pg. 218-234, 2000.

19. Lorenz, R.D., "Titan Here We Come," *New Scientist*, Vol. 167, No. 2247, July 15, 2000.

20. Lorenz, R.D., "Flexibility for Titan Exploration: The Titan Helicopter," *Forum on Innovative Approaches to Outer Planetary Exploration 2001-2020*, Lunar and Planetary Institute (LPI) Report # 1084, Houston, TX, February 21-22, 2001.

21. Nishimura, J., et al, "Venus Balloons at Low Altitudes," *Advances in Space Research*, Vol. 14, No. 2, Great Britain, 1994.

22. Lodders, K. and Fegley, Jr., B., *The Planetary Scientist's Companion,* Oxford University Press, 1998.

23. Selig, M., Donovan, J., and Fraser, D., *Airfoils at Low Speeds*, H.A. Stokely. Publisher, 1989.

24. Lorenz, R., and Milton, J., *Lifting Titan's Veil: Exploring the Giant Moon of Saturn*, Cambridge University Press, 2002.

25. Abrego, A., Chang, I., and Bulaga, R., "Performance Study and CFD Predictions of a Ducted Fan System," AHS Specialist's Meeting on Aerodynamics, Acoustics, and Test and Evaluation, San Francisco, CA, January 23-25, 2002.

26. Van Weelden, S.D., Smith, D.E., Mullins, B.R. Jr., "Preliminary Design of a Ducted Fan Propulsion System for General Aviation Aircraft," AIAA Paper 96-0376, AIAA 34th Aerospace Sciences Meeting and Exhibit, Reno, NV, Jan 15-18, 1996.

27. Cahn, M.S., "The Design and Performance of Shrouded Propellers," National Aerospace Engineering and Manufacturing Meeting, Society of Automotive Engineers, Paper 587C, Los Angles, CA, October 8-12, 1962.

28. Kjerstad, K.J., Paulson, J.W. Jr., "Transition Aerodynamics for 20-Percent-Scale VTOL Unmanned Aerial Vehicle," NASA Technical Memorandum 4419, April 1993.

29. Anderson, S.B., "An Overview of V/STOL Aircraft Development," AIAA Paper 83-2491, AIAA Aircraft Design, Systems, and Technology Meeting, Fort Worth, TX, Oct 17-19, 1983.

30. Cook, W. L., "Summary of Lift and Lift/Cruise Fan Powered Lift Concept Technology," NASA Contractor Report 177619, August 1993.

31. Lehman, C., Crafa, V., "Nacelle Design for Grumman Design 698 V/STOL," .

32. Wilson, S.B., III, Donley, S, et al., "Handling Characteristics of a Simulated Twin Tilt Nacelle V/STOL Aircraft," .

33. Kohn, J., "Aerodynamics, Propulsion, and Longitudinal Requirements for a Tilt-Nacelle V/STOL with Control Vanes Submerged in the Nacelle Slipstream," .

34. Mort, K. W., "Summary of Large-Scale Tests of Ducted Fans," NASA Conference on V/STOL and STOL Aircraft, Paper # 8, NASA Ames Research Center, Moffett Field, CA, April 4-5, 1996.

35. Maki, R. L. and Giulianetti, D. J., "Aerodynamic Stability and Control of Ducted Propeller Aircraft," NASA Conference on V/STOL and STOL Aircraft, Paper # 9, NASA Ames Research Center, Moffett Field, CA, April 4-5, 1996.

36. Hall, E. J. and Delaney, R. A., "3D Euler Analysis of Ducted Propfan Flowfields," AIAA Paper # 90-3034, AIAA 8th Applied Aerodynamics Conference, Portland, Oregon, Aug 20-22, 1990.

37. McCormick, B.W., Jr., *Aerodynamics of V/STOL Flight*, Academic Press, New York, 1967.

38. Omar, M.E. and Lampkin, B.A., "Tenth-Scale Powered Model Test of a Tilt-Nacelle V/STOL Airplane," AIAA Paper 77-594, AIAA/NASA Ames V/STOL Conference, Palo Alto, CA, June 6-8, 1977.

39. Titan Vertical Lift Aerial Vehicle Student Design Competition: http://www.integratedspacetechnologies.com/titan/

40. Johnson, W.R., *Helicopter Theory*, Princeton University Press, 1980.

41. Stepniewski, W.Z. and Keys, C.N., *Rotary-Wing Aerodynamics*, Dover Publications, Mineola, NY, 1984.

42. Coleman, C.P., "A Survey of Theoretical and Experimental Coaxial Rotor Aerodynamic Research," NASA TP-3675, 1997.

43. NASA Astrobiology Science and Technology for Exploring Planets Announcement of Opportunity: http://research.hq.nasa.gov/code_s/nra/current/NRA-02-OSS-01-ASTEP/index.html

44. Young, L.A., Johnson, J.L., Andrews, J., and Demblewski, R., "New Concepts and Perspectives on Micro-Rotorcraft and Small Autonomous Rotary-Wing Vehicles,"20th AIAA Applied Aerodynamics Conference, Saint Louis, MO, June 24-27, 2002.

Appendix A – Mars Rotor Hover Test Performance Data Reduction

Rotor thrust for the Mars rotor hover testing was measured by combining the output of three calibrated load cells. Rotor collective was measured by performing an installed calibration of the control system actuator tachometer. Both rotor thrust and collective were relatively straightforward to measure. Rotor power required additional effort to acquire an accurate set of measurements.

Initial hover testing of the Mars baseline rotor was conducted with electric motor manufacturer-specified "torque constants" to estimate rotor shaft torque and power during testing. Though this was an acceptable approach for rotor operation during testing, it was unacceptable for deriving accurate research-quality measurements of the rotor performance. An accurate estimate of the motor torque constant needed to be derived.

The equation relating the motor torque constant to rotor shaft torque and motor input voltage is given by

$$Q = K_T K_I V_i \qquad (1)$$

Where Q is the rotor shaft torque, the torque constant is K_T, the amplifier gain constant is K_I, and V_i is the current-related motor controller voltage.

A post-test methodology was developed to obtain accurate measurements of the installed test stand motor torque-constant, as well as to acquire bare shaft tares for the rotor. To achieve this objective a series of installed (in the hover test stand) electric motor tests were conducted. One set of test results was acquired for the test stand with a bare rotor output shaft. A second set of test results were acquired for the test stand and installed electric motor by installing (on the test stand output shaft) and spinning a metal disk of known inertia. For both sets of test data (with and without the inertia disk), the motor solid-state controller was programmed to vary the rotor speed in linear increasing/decreasing ramps in speed for several cycles – thus approximating a nearly constant motor acceleration/deceleration of known magnitude. By matching the motor acceleration/deceleration profiles (with and without the inertia disk) with instantaneous motor electrical measurements, an installed motor torque constant could be derived, as well as a more accurate estimate of the motor inertia (Fig. 32).

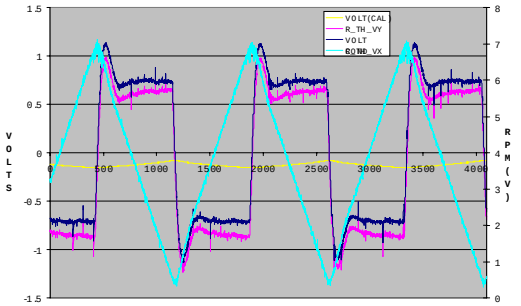

Fig. 32 – Sample Motor Voltage and RPM versus Time

Mathematically, this "inertia disk" acceleration and deceleration approach to deriving the motor torque constant is summarized in the following discussion.

The corrected torque constant, K_{Tv}, can then be calculated from the torque equations for a bare shaft (Configuration 1) and with the inertia disc (Configuration 2) with the following derivations.

The applied torque due to the bare shaft acceleration is given by the expression:

$$Q_{acc1} = \alpha_1 I_o \qquad (2)$$

Where a is the motor acceleration with a bare-shaft and I_o is the unknown, actual, moment of inertia for the motor and bare-shaft configuration.

The measured torque is given by

$$Q_{volt1}=K_T K_I V_{i1} \quad (3)$$

Correspondingly the applied torque due to inertia disk acceleration is:

$$Q_{acc2}= \alpha_2(I_o + I_{disc}) \quad (4)$$

Finally, the measured torque due to disk acceleration is given by:

$$Q_{volt2}=K_T K_I V_{i2} \quad (5)$$

Now

$$Q_{acc1}= Q_{volt1} \quad (6)$$

And

$$Q_{acc}2= Q_{volt}2 \quad (7)$$

Finally, noting that the product of the torque constant, K_T, and amplifier gain constant, K_I, is given by the expression:

$$K_{Tv} = K_T K_I \quad (8)$$

And so performing the appropriate algebra yields

$$K_{Tv} = \alpha_2 I_{disc}/[V_{i2} - V_{i1}(\alpha_2/\alpha_1)] \quad (9)$$

This process is repeated for several different accelerations and an average estimate is used to define installed/corrected torque constant.

The expression for the corrected motor torque constant, K_{Tv} is independent of the motor moment of inertia, I_o. The corrected, or rather actual, motor moment-of-inertia, I_1, can, though, be derived from the above set of equations as:

$$I_1 = (\alpha_2 I_{disc}) [\alpha_1(V_{i2}/V_{i1}) - \alpha_2] \quad (10)$$

Through this methodology, an installed motor torque constant was derived that was 19% higher than the manufacturer-specified value. The derived motor inertia value was 7% higher than the manufacturer specification.

Appendix B – "Titan VTOL" Unducted- and Ducted-Fan Hover Test Performance Data Reduction

To conduct the aerodynamic hover performance configuration studies of terrestrial surrogate vehicles for a Titan VTOL, two-bladed rotors having a solidity of 0.091, tapered-blade planform, and flat-plate circular-arc airfoils were used during the hover testing. Further, the rotor blades were at fixed-pitch and rotor thrust and power was varied solely by rotor shaft RPM increases. The rotor blades were cantilevered from the hub and were of very low stiffness. Though these rotors are not representative of the design/construction of rotors/fans that would be employed in a Titan VTOL vehicle, they allowed an opportunity using simple models to assess influence of rotor configuration effects on fundamental rotorcraft performance characteristics. In particular, the focus of the research being on the effect of dual-rotor configurations of rotor thrust and power as related to isolated rotor performance characteristics.

To test the rotors, a hover test stand was constructed. A hollow 2.54 cm square-stock aluminum bar was mounted on bearings inside of a 8.9 cm diameter, aluminum horizontal support tube. The inner aluminum bar rode on tracked roller bearings and was attached to the load cell at the far end (with respect to the rotor apparatus) of the horizontal support tube. Figure 33 shows the hover test stand.

Fig. 33 -- Test Stand (Unducted-Fan Testing)

The two rotors were mounted on the end of 1.27 cm diameter carbon rods. These "swing arms" were mounted to circular clamps that could be loosened by a single bolt to allow easy repositioning of the arms and the two rotors. By horizontally translating and rotating the "swing arms" the relative position of the two rotors could be varied. This technique was employed to test coaxial and tandem rotor configurations (both ducted and unducted).

A DC power supply was utilized to power the two rotors. The motors were wired in parallel to the power supply. RPM for the rotors was varied by adjusting the voltage output of the power supply. Blade pitch remained fixed for each rotor. Rotor speed was measured by an optical tachometer. Total rotor thrust was measured by a calibrated load cell affixed at the end of the test stand's horizontal support tube. Rotor shaft power was derived via estimates of the rotor/drive-train efficiency made through rotor bat testing and the methodology

outlined in Ref 44. Figure 34 is the motor/drive-train efficiency curve derived from four sets of varying rotor bat lengths.

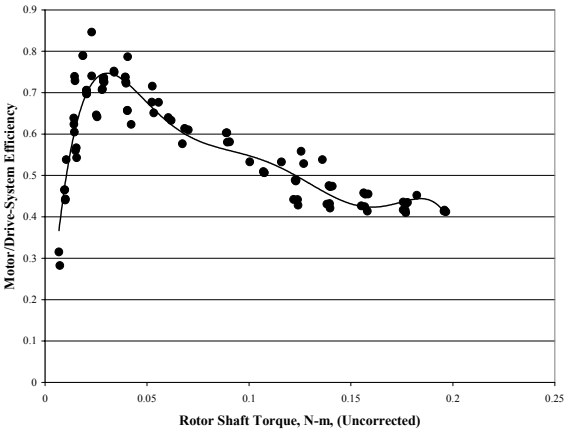

Fig. 34 – Motor/Drive-Train Efficiency as a Function of Motor Torque Loading

Both hub tares and the motor drive train efficiency were made to the rotor data. No test stand interference corrections were made to the rotor data. The efficiency correction is:

$$P = P_{Input}\, f\left(\frac{P_{Input}}{\Omega}\right) - P_{HT_{Input}}\, f\left(\frac{P_{HT_{Input}}}{\Omega}\right) \qquad (11)$$

where P is the rotor shaft power corrected for hub tares (all data in the paper have hub tares applied), P_{Input} is the motor/drive-train input (electrical) power at the rotor test condition, $P_{HT_{Input}}$ is the hub tare input (electrical) power. The form of the efficiency function, *f*, is derived from regression analysis of Fig. 34 data.

Both isolated rotor and dual-rotor data were acquired. Isolated rotor and dual-rotor performance measurements were compared to each other by dividing the dual rotor data by a factor of two. Because input electrical power was provided in parallel to both rotors (and two independent motor/drive-trains) when in dual-rotor operation, the rotor speeds – though individually measured – varied upon test condition with respect to each other. The disagreement between the two rotor speeds was typically 5% of the nominal operating speed. To account for the difference between the two rotor speeds for a given test condition, a root-mean-square ($\Omega = \sqrt{(\Omega_1^2 + \Omega_2^2)/2}$) estimate of a nominal rotor speed was employed to estimate rotor thrust and power coefficients and figure of merit.
Figures 35a-c are pictures of a few of the unducted dual-rotor configurations studied.

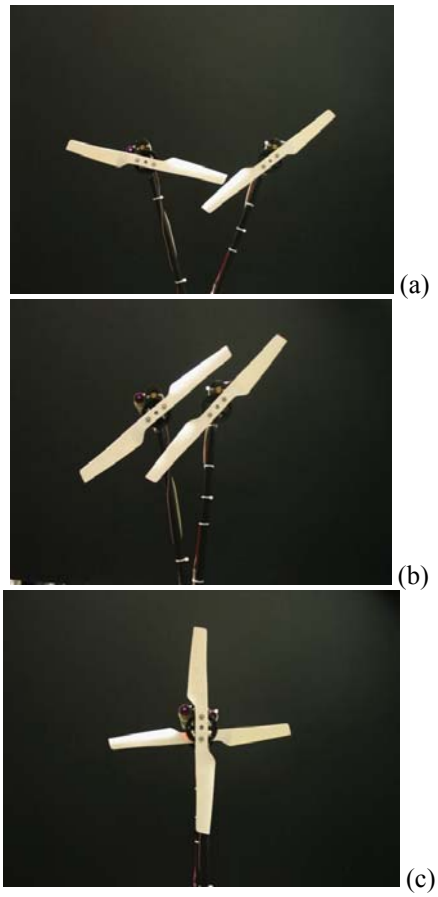

Fig. 35 – Examples of Unducted Rotor Configurations (h/R = 0.617): (a) s/R = 0.69, (b) s/R = 0.345, and (c) s/R = 0

Because rotor thrust and power could only be varied by rotor speed changes for the testing conducted (versus having control over rotor collective), this presented challenges to the analysis of the rotor data. Figure 36a-b is an illustrative example of rotor data from the unducted rotor/fan hover testing for a isolated rotor and a coaxial rotor (thrust and power divided by two) configuration.

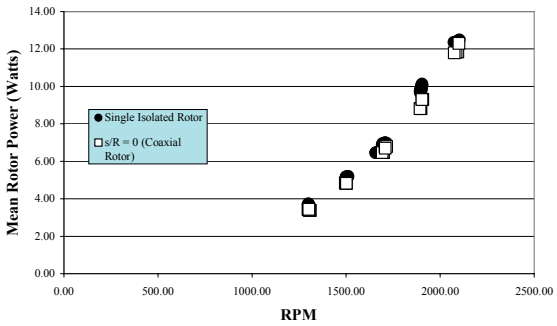

(a)

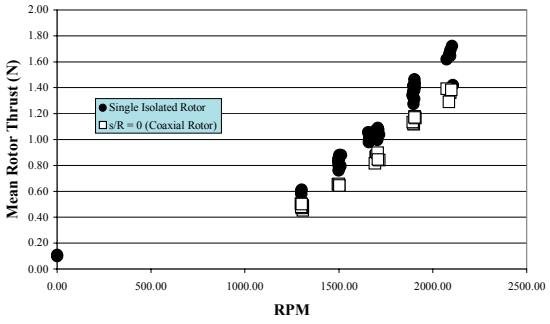

(b)

Fig. 36 – Typical (a) Power and (b) Thrust Data as a Function of Rotor RPM

Ideally, because the rotor blades are flat-pitch, the rotor thrust and power coefficients should be constant with rotor speed. Reynolds number effects only make this true for performance data at higher tip Reynolds numbers. Figure 37 shows the nominal observed effects of rotor tip Reynolds number on rotor thrust and power coefficients. Analysis of the data was therefore limited to the higher tip speeds when comparing rotor configurations.

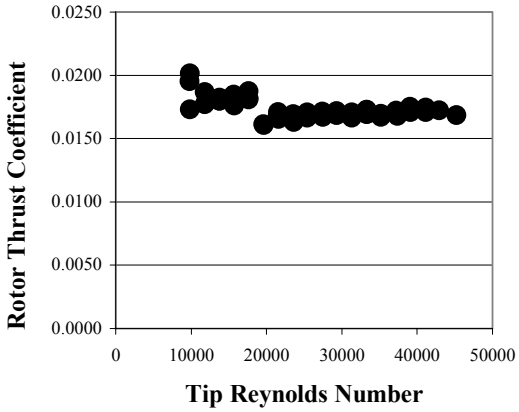

(a)

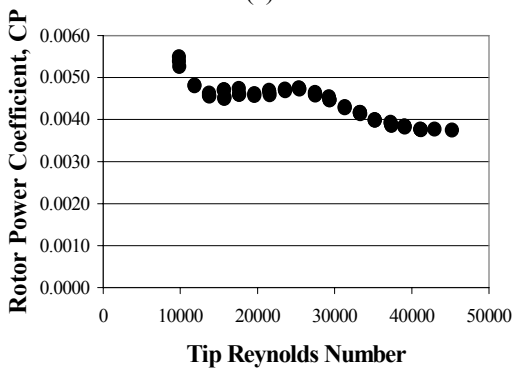

(b)

Fig. 37 – Typical Tip Reynolds Number Effect on (a) Thrust Coefficient and (b) Power Coefficient

Comparison of rotor performance between the various rotor configurations was accomplished by nondimensionalizing the thrust or power measurements of one configuration by those of a second configuration. For the unducted fan/rotor measurements the ratios of mean rotor thrust to isolated rotor thrust, T/T_I, and the ratio of mean rotor power to isolated rotor power, P/P_I, were compared as a function of parametric sweeps of s/R, the longitudinal rotor separation, and h/R, the rotor vertical separation distance. Obtaining these nomdimensional performance ratios was based as following manner.

If the rotor thrust and power coefficients are constant with respect to rotor speed (ideally true for fixed-pitch rotor blades, but found to be true only for tip Reynolds greater than 30,000 for the rotors tested), then rotor power and thrust for two separate configurations (1 and 2) are simple functions of rotor speed:

Configuration 1 Configuration 2

$$\frac{T_1}{\rho} = a_1\Omega^2 \quad \text{and} \quad \frac{T_2}{\rho} = a_2\Omega^2$$

$$\frac{P_1}{\rho} = b_1\Omega^3 \quad \text{and} \quad \frac{P_2}{\rho} = b_2\Omega^3$$

(12a-d)

Having acquired thrust and power data as a function of rotor speed, such as in Fig. 36, simple least-squares regression analysis can be employed to derive estimates of the speed relationship coefficients, for any given rotor configuration.

$$a = \frac{\sum_{i=1}^{n}\left(\frac{T_i}{\rho_i}\right)\Omega_i^2}{\sum_{i=1}^{n}\Omega_i^4} \qquad b = \frac{\sum_{i=1}^{n}\left(\frac{P_i}{\rho_i}\right)\Omega_i^3}{\sum_{i=1}^{n}\Omega_i^6}$$

(13a-b)

Now configuration 1 and 2 can be arbitrary in nature and one could use the above relationships to compare mean thrust or power of a dual-rotor configuration to isolated rotor performance (P/P_I and T/T_I), or, alternatively, one could be comparing ducted-fan dual-rotor performance to unducted-fan performance (P_{DF}/P_{UDF} and T_{DF}/T_{UDF}). Both types of comparisons are made in this paper using this general "ratio" approach of comparing the performance of two different rotor configurations.

$$\frac{T_2}{T_1} = \frac{a_2}{a_1}$$ (constant collective and rotor speed)

$$\frac{P_2}{P_1} = \left(\frac{b_2}{b_1}\right)\left(\frac{a_1}{a_2}\right)^{3/2} \quad \text{(constant thrust coefficient)}$$

$$\frac{T_2}{T_1} = \left(\frac{a_2}{a_1}\right)\left(\frac{b_1}{b_2}\right)^{2/3} \quad \text{(constant power)}$$

(14a-c)

In order to compare analytical predictions of induced power for various configurations to the experimental results, it was necessary to derive estimates of the profile power coefficient, C_{P0}, to therefore estimate induced power. This could not be accomplished through regression analysis of the isolated rotor nondimensional C_P and C_T polars because of the used of fixed-pitch rotor blades. (Ideally, for fixed-pitch blades, C_T and C_P are constants, and, therefore, insufficient information would exist to derive independent estimates of C_{P0} and k). An alternate regression analysis approach was taken wherein the use of the dimensional values of rotor thrust and power (as varied with rotor speed) were used to define the least-squares error function.

The least-squares error function, E, was defined as

$$E = \sum_i \left[P_i - \left(k\sqrt{\frac{T_i^3}{2\rho_i A}} + C_{P0} A R^3 \rho_i \Omega_i^3 \right) \right]^2$$

(15)

From this least-squares regression analysis error function, the following coefficients can be defined

$$A_1 = \frac{1}{\sqrt{2A}} \sum_i \frac{T_i^3}{\rho_i} \qquad A_2 = \frac{1}{\sqrt{2A}} \sum_i \Omega_i^3 \sqrt{\rho_i T_i^3}$$

$$B_1 = AR^3 \sum_i \Omega_i^3 \sqrt{\rho_i T_i^3} \qquad B_2 = AR^3 \sum_i \left(\rho_i \Omega_i^3\right)^2$$

$$C_1 = \sum_i P_i \sqrt{\frac{T_i^3}{\rho_i}} \qquad C_2 = \sum_i P_i \rho_i \Omega_i^3$$

(16a-f)

Where

$$C_{P0} = \left(C_1/A_1 - C_2/A_2\right)/\left(B_1/A_1 - B_2/A_2\right)$$

$$k = \left(C_1/B_1 - C_2/B_2\right)/\left(A_1/B_1 - A_2/B_2\right)$$

(17a-b)

A is the rotor disk area and R is the rotor radius. A profile drag coefficient of C_{P0}=0.00052 and an induced power constant of k=2.07 were derived from the isolated rotor data set (for tip Reynolds numbers greater than 30,000).

The electrical input power to the dual rotor configurations was provided in parallel to the two electric motors. A speed difference of approximately 5% was typically observed between the two rotors. This rotor speed difference translated to a rotor load share imbalance for some of the test results, particularly the unducted coaxial rotor configurations. A load share correction was applied to the unducted coaxial rotor data. Only total thrust was measured on the hover test stand, and, so, the load share had to be inferred from the rotor speed measurements during the testing. Noting that for the fixed-pitch rotors that C_T is constant for both rotors, then

$$\tau \equiv T_1/T_2 \propto \left(\Omega_1/\Omega_2\right)^2 \qquad (18)$$

The first-order rotor load share correction applied was then, therefore

$$\left.\frac{P}{P_1}\right|_{\substack{\text{Induced Power,}\\ \text{Corrected}}} = \left(\frac{2}{1+\tau}\right)^{3/2} \cdot \left.\frac{P}{P_1}\right|_{\substack{\text{Induced Power,}\\ \text{Uncorrected}}} \qquad (19)$$

Corrections ranging from 5 to 10% were typically applied to the unducted coaxial rotor data. All other dual rotor data in the paper have been presented uncorrected, with respect to rotor load share.

Appendix C – Additional Notional Planetary Mission Background

Mars Explorations

References 9 and 15 have devoted a fair amount of discussion related to robotic Mars exploration missions employing rotorcraft as aerial explorers. Two early candidate missions, in particular, have been studied: an aerial surveyor and soil/rock sampler mission, and a rover and micro-scout combination (Fig. 38a-b).

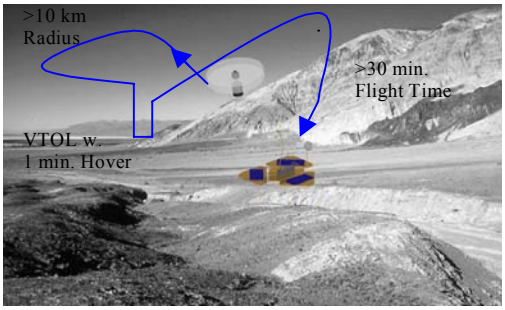

(a)

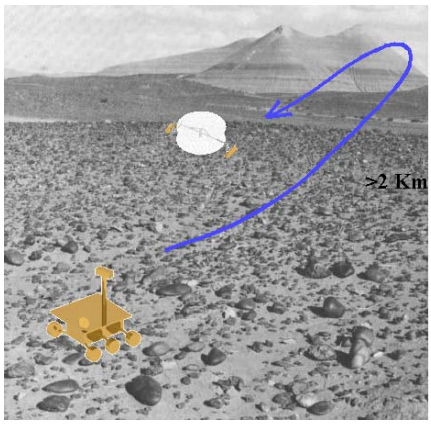

(b)

Fig 38 – Mars Rotorcraft Missions (a) Soil/Rock Sample Return to Lander and (b) Micro-Scout for Large Rovers

Titan

The exploration of the solar system outer planets has several unique challenges as compared to missions to the inner planets. Among those challenges are the near-mandatory use for onboard nuclear power generation for spacecraft operation, the effect of spacecraft remoteness on telecommunication and mission execution, the long duration of mission length, etc. Among the many questions a mission planner has to answer are the ones listed in Table 2.

Table 2 – Sample List of Mission Planning Questions

Notional Mission Characteristics	Constraints, Considerations, & Comments
What are the Mission science goals?	
High-resolution imaging of Titan surface to characterize geological processes and planetary body evolution Multiple remote site surface samples over a wide area to perform pre-biotic organic chemistry survey In-flight, variable (low to medium) altitude atmospheric sampling to characterize atmospheric constituents and aerosol particle dynamics and evolution	In-flight aerial imagery can complement panoramic ground images acquired at remote landing sites; both sets of aerial vehicle images can be complemented with high-altitude orbiter imagery Mobility afforded by a VTOL aerial vehicle is essential to acquire multiple site surface samples and return to lander for detailed analysis
What are the major science instruments?	
Orbiter: Radar & IR Imaging Lander: Gas Chromatograph Mass Spectrometer; micro-imager; upward-projecting Lidar for atmospheric turbulence measurements; temperature and pressure sensors; seismometers Aerial Vehicle: Optical imager with pan and telephoto; surface and atmospheric sampling devices; penetrometers on landing gear; laser ablation mass spectrometer	Acquiring data regarding the topology of Titan's surface, couple with an intensive multiple site sampling measurement of Titan's surface (and atmospheric) chemistry is paramount to the understanding of the formation and evolution of this planetary body. Further, seismic and atmospheric wind/turbulence measurements would enable an understanding of the transport mechanisms for the atmospheric and surface chemical constituents.
What are the major spacecraft elements?	
Cruise-Phase Spacecraft/Carrier Platform Orbiter EDLS & Lander	Carrier transports orbiter and EDLS/Lander to Titan insertion; Saturn flyby opportunity post-orbiter and EDLS release Orbiter required to provide telecom support for Lander and aerial vehicle; secondary capability is to provide on-orbit imagery of Titan's surface Lander acts as delivery system and post-landing primary base for aerial vehicle support; lander would also have in-situ sample analysis capability for sample returned by the aerial vehicle Lander would carry nuclear power source and would recharge aerial vehicle batteries and/or fuel-cell
Aerial Vehicle	
Power Requirements?	
Cruise-phase carrier platform/spacecraft would carry one to two nuclear power sources Orbiter would rely on batteries/fuel-cells and tethered satellite electric power generation capability Lander would have to carry one nuclear power source Aerial vehicle would rely on batteries and/or fuel cells which would be recharged by the lander	Innovative technologies will be required to keep number of nuclear power sources to a minimum Aerial vehicles will be energy intensive platforms that will require long recharge periods of time between flights
Telecommunication Requirements?	
Orbiter would be primary telecom link between lander and aerial vehicle and Earth Lander would be capable of low-bandwidth direct contact with Earth, as a contigency capability Aerial vehicle would be able to communicate with lander via the orbiter; no direct telecom to Earth	Titan and Saturn's considerable distance from Earth, coupled with the high data bandwidth required for a Titan VTOL aerial explorer mission will pose significant deep-space communication challenges. This challenge can be somewhat moderated by incorporation of an orbiter into the baseline mission for orbital observations and telecom relay to Earth of the ground assets.
Anticipated Duration of Mission?	
Six months post-Titan orbital insertion and entry/descent	Mission duration will be dictated by two primary constraints: operations support limits/costs, and predicted mean time between equipment failures and projected cumulative probabilities of flight incidents/accidents with time.
What is the target in-atmosphere survey area to be covered, or flight endurance to be achieved?	
A minimum radius of action of 150 to 200 kilometers should be required	A wide survey area and multiple flights/sorties should be supported by the baseline mission to acquire a scientifically valid survey of the planetary body
What is the level of autonomy and "robotic cooperation" required for the Mission?	
High levels of Aerial Vehicle and Lander Autonomy Required Lander acts a Primary Base for Aerial Vehicle High level of robotic cooperation: Lander provides support and post-flight in-situ analysis for aerial vehicle	A "system of systems" approach will need to be taken to establish required technical readiness levels for flight hardware. This will include extended duration robotic aerial explorer and lander surrogate demonstrations at remote extreme environment terrestrial sites.
What level of "heritage" can be applied to the mission?	
Cruise-Phase Carrier Platform & EDLS can be scaled-up from Cassini-Huygens mission. Aeroassist maneuvers from Mars Global Surveyor Inflatable structures for aerobraking/aeroassist from Russia/ESA IRDT Flight Demo 2000 Tethered Satellite technology from NASA/ASI TSS-1R mission on STS-75	
What are the critical technologies required to execute the Mission?	
Aerial Vehicle Design	Ground test facilities can be developed to test key aerial vehicle technologies.

Orbiter aeroassist orbital entry using inflatable structures Orbiter tethered satellite electrical power generation Improved nuclear power sources for cruise-phase carrier platform and the lander/aerial vehicle combination System Automation	Remote site terrestrial extreme environment robotic aerial explorer and lander surrogate demonstrations will conducted to validate system automation technical readiness.

The notional mission characteristics noted in Table 2 for a Titan aerial explorer are illustrated in part in Fig. 39a-d.

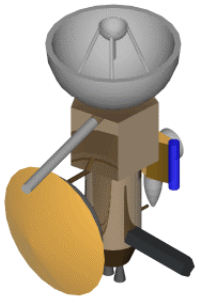

(a)

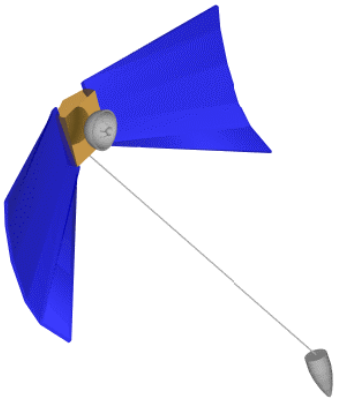

(b)

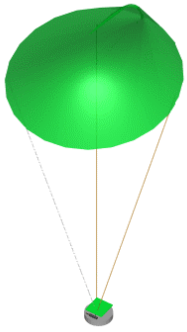

(c)

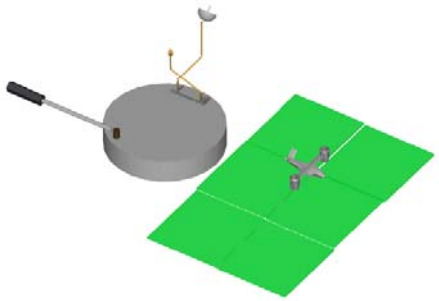

(d)

Fig. 39 – Titan VTOL: (a) spacecraft, (b) orbiter with aerobrake inflatable structures and electrical generation tether, and (c) EDLS descent, and (d) aerial explorer & lander

Venus

Exploring Venus, as an inner planet in the solar system, is somewhat easier than missions to Titan in some regards, but in other ways the problem is even more challenging. Though closer to Earth, and having abundant solar energy (while outside the Venus's atmosphere), the atmospheric conditions near, or on, Venus' surface are extremely harsh.

Table 3– Venus Hybrid Airship Mission Planning Questions

Notional Mission Characteristics	Constraints, Considerations, & Comments
What are the Mission science goals?	
To investigate the near-surface atmospheric dynamics and constituents of Venus Acquire multiple site ground images and limited surface sample chemical/geological in-situ analyses Acquire "ground truth" of Magellan and orbiter radar imagery for small limited areas	It is essential from a scientific standpoint to uncover the similarities and differences between the planetary evolutionary processes of Venus versus Earth.
What are the major science instruments?	
Orbiter: ground penetrating radar Aerial Vehicles: APXS mass spectrometer for surface samples; pressure and temperature sensors; seismometer probes; radar imaging; micro-imager; gas chromatograph mass spectrometer for atmospheric samples	The primary focus of the orbiter and powered-flight phase of the aerial vehicles would be to better understand the geology and mineralogy of Venus' surface. The unpowered-flight phase of the aerial vehicles would be dedicated to understanding the low and medium atmospheric chemistry and transport mechanisms.
What are the major spacecraft elements?	
Combination cruise-phase carrier platform and orbiter Two EDLS systems, each carrying one aerial vehicle	Multiple EDLS and aerial vehicles increases mission science return and/or mitigates risk Having both a powered and unpowered (drift) stage to the aerial vehicles flight profile would extend flight endurance and mission science return
Power Requirements?	
Solar arrays for orbiter/spacecraft High temperature batteries for aerial vehicles	Use of solar cell arrays would reduce mission cost

Aerial vehicle propulsion options include electric drives or heat (possibly steam) engines	
Telecommunication Requirements?	
Aerial vehicles would be capable of telecom with orbiter and directs links with Earth	
Anticipated Duration of **Mission?**	Per aerial vehicle: 30-60 minutes powered flight near Venus' surface; 2-3 days drifting unpowered at medium altitudes after jettisoning ballast and unessential hardware post-powered flight.
What is the target in-atmosphere survey area to be covered, or flight endurance to be achieved?	Fifty kilometers of total range with on to two soft landings on surface
What is the level of autonomy and "robotic cooperation" required for the Mission?	
What level of "heritage" can be applied to the mission?	
Cruise-Phase Platform & Orbiter can be scaled-up from Magellan spacecraft EDLS & Lander technology from USSR Venera 9 and 13	
What are the critical technologies required for the Mission?	
High temperature electronics, materials, and propulsion systems for aerial vehicles Multiple EDLS release from a single spacecraft/orbiter	Improvements in high temperature electronics and other equipment will be essential for unpowered flight phase and/or alternatively a final soft landing to conclude mission. Because of the extreme environmental conditions of Venus' surface vehicle recharging and multiple flight/sorties from a lander is unlikely – thus making a Venus aerial explorer mission inherently different in character from a Mars or Titan mission. Limitations in powered flight duration and equipment longevity in the Venusian near-surface atmosphere can partially be compensated for by employing multiple aerial vehicles for the overall mission.

The notional mission characteristics noted in Table 3 for a Venus hybrid airship are illustrated in part in Fig. 40a-c.

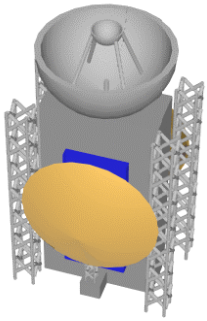

(a)

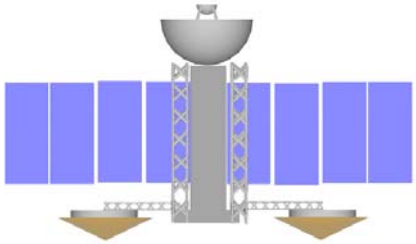

(b)

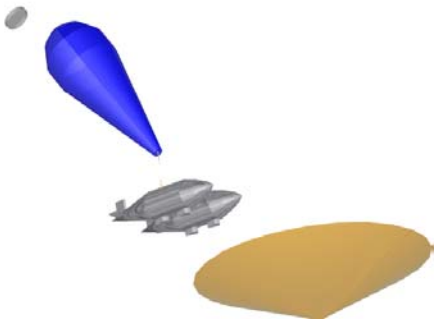

(c)

Fig. 40 – Notional Mission: (a) spacecraft at launch, (b), spacecraft in orbital insertion configuration, and (c) entry and descent of the Venus hybrid airship explorers

Appendix D – Momentum and Vortex Theory Models

Unducted Coaxial Rotor Induced Power

Assume that a coaxial rotor system has the upper rotor located at z/R = + h/R and the lower rotor at z/R=0. The induced power ratio of an unducted coaxial rotor (with respect to isolated rotor induced power) can be expressed by the following expression:

$$\left.\frac{P}{P_I}\right|_{Induced\ Power} = \frac{T_U v_{Uh} + T_L \bar{v}}{\sqrt{T^3/2\rho A}} \qquad (20)$$

T_U and v_U is the upper rotor thrust and induced velocity at the upper rotor's disk plane. T_L is the lower rotor thrust. Note that the total thrust can be related to the individual rotor thrust by the expression

$$T = (\tau + 1)T_L \qquad (21)$$

The above expression introduces the rotor load share factor, τ, such that $T_U = \tau T_L$. Also introduced is the velocity term, $\bar{v}$, which is an (rotor disk) area-weighted "mean" induced velocity through the lower rotor's disk plane.

Substituting Eq. 20 into 21 gives

$$\left.\frac{P}{P_I}\right|_{Induced\ Power} = \frac{1}{(1+\tau)^{3/2}}\left(\tau\nu_{Uh} + \bar{\nu}\right)\sqrt{\frac{2\rho A}{T_L}} \tag{22}$$

To proceed further in the analysis, three assumptions now have to be made. First, the single isolated rotor induced velocity distribution can be approximated by actuator disk vortex theory (where the rotor wakes are approximated by vortex cylinders, and superposition of induced velocities is allowed). Second, the upstream/upper rotor's wake contraction (as it intersects the downstream/lower rotor's disk plane) can be approximated by applying mass flow continuity to the above vortex cylinder velocity distribution. And, finally, third, an area-weighted "mean" (spatially averaged across the whole rotor disk) inflow velocity can be defined for the downstream/lower rotor taking into account the upstream rotor's wake. These three assumptions can be encompassed by the following set of equations:

$$\nu(\vartheta, z/R)\big|_{Single\ Rotor} \approx \frac{\gamma}{2}\left[1 - \frac{(z/R - \vartheta)}{\sqrt{1+(z/R-\vartheta)^2}}\right] \tag{23a}$$

(Where $\vartheta = h/R$ and $\gamma=\gamma_U$ for the upstream/upper rotor, and $\vartheta = 0$ and $\gamma=\gamma_L$ for the downstream/lower rotor. Correspondingly, referring to Eq.23a, $\nu_{Uh} \equiv \nu(h/R, h/R) + \nu(0, h/R)$; $\nu_{U0} \equiv \nu(h/R, 0)$; $\nu_L \equiv \nu(0, 0)$.

$$A_{Wake} \approx \frac{\pi R^2}{\left[1 + \frac{h/R}{\sqrt{1+(h/R)^2}}\right]} \tag{23b}$$

$$\bar{\nu} \equiv \sqrt{\left(\frac{A_{Wake}}{\pi R^2}\right)\left(\nu_{U0} + \nu_L\right)^2 + \left(1 - \frac{A_{Wake}}{\pi R^2}\right)\nu_L^2} \tag{23c}$$

The definition and usage of $\bar{\nu}$ in Eqs. 20 and 23c is more than a mathematical artifice. This area-weighted "mean" induced velocity at the downstream/lower rotor's disk plane can be thought of as accounting for the mixing/transport of momentum from the inner portion of the downstream rotor disk (where the upstream rotor wake is initially entrained) to the outer portion of the disk (which is ostensibly, at least by classic rotor momentum theory, unaffected by the upstream rotor).

Noting that $C_T = T_L/\rho A V_T^2$, $\gamma_U = \tau V_T\sqrt{2C_T}$ and $\gamma_L = V_T\sqrt{2C_T}$, then Eqs. 23a-c can be substituted into Eq. 22 and the resulting induced power ratio solution can be derived as

$$\left.\frac{P}{P_I}\right|_{Induced\ Power} = \frac{1}{(1+\tau)^{3/2}}\left[\tau f + \sqrt{2\sqrt{\tau}+1+\tau g}\right]$$

Where

$$\zeta = \frac{h/R}{\sqrt{1+(h/R)^2}}$$

$$g = 1 + \zeta$$

$$f = 2 - \zeta \tag{24a-d}$$

Equation 24 agrees with the momentum theory solution (for example, Ref. 40) for h/R=0, i.e. $P/P_I \to \sqrt{2} \approx 1.41$. However, the derived approximate vortex theory result deviates from the momentum theory solution for when h/R is very large. In this case, as h/R increases the momentum theory would suggest that P/P_I asymptotically approaches 1.28, versus the derived approximate vortex theory result which yields $P/P_I \to 1.144$ (for a rotor load share τ=1). The coaxial rotor momentum theory result, for large h/R, suffers from the assumption that the flow can be divided into two distinct regions: the inner half of the lower/downstream rotor disk area where the upstream rotor wake is entrained, and the outer half of the rotor disk area which operates without being influence by the upstream rotor. This assumption results in too simplistic modeling. Neither momentum theory, or the simple approximate vortex theory presented in this paper, accounts for the effects of rotor wake viscous diffusion in the far wake wherein at some point $h/R \to \infty$ and $P/P_I \to 1$, though the vortex theory does a better job of approaching that limit. Largely unexplored in this paper is the effect of non-unity rotor load share on P/P_I. Note that the derived approximate vortex theory does correctly predict that if τ=0 then P/P_I=1.

Elliptical/Oval Duct Thrust/Lift Augmentation

The "static thrust," or rather hover, induced power of a ducted fan is (Ref. 27)

$$P_{DF} = \sqrt{\frac{T^3}{2\rho_e A_e}} \qquad (25)$$

The effective duct exit density, and exit area, are given by ρ_e and A_e. For a low-pressure-ratio ducted fan: $\rho=\rho_e$ and $A_e=A_{DF}$. Note that for an "ideal" oval ducted fan $A_{DF} = \pi R^2 + 2sR$

From Ref. 40, the induced power of an unducted tandem rotor configuration, and an isolated rotor, is each respectively given by

$$\left.\frac{P_{UDF}}{P_I}\right|_{Induced\ power} = \left(\frac{2}{2-m}\right)^{1/2} \qquad (26a)$$

Where the dual-rotor overlap, m, is given by

$$m = \frac{2}{\pi}\left[\cos^{-1}\left(\frac{s}{2R}\right) - \left(\frac{s}{2R}\right)\sqrt{1-\left(\frac{s}{2R}\right)^2}\right] \qquad (26b)$$

And

$$P_I = \sqrt{\frac{T^3}{2\rho A}} \qquad A = \pi R^2 \qquad (26c\text{-}d)$$

Substituting the above equations into the ducted fan induced power expression, and solving for the power ratio P_{DF}/P_{UDF} gives

$$\left.\frac{P_{DF}}{P_{UDF}}\right|_{Induced\ Power} = \sqrt{\left(\frac{2-m}{2}\right)\left(\frac{\pi R^2}{A_{DF}}\right)} \qquad (27)$$

Now for a "real" oval ducted fan, introducing the ducted fan "efficiency," ε, the oval ducted fan effective exit area, A_{DF}, is given by the expression

$$A_{DF} = \left(\frac{2-m}{2}\right)\pi R^2 + \varepsilon\left[\left(\frac{2+m}{2}\right)\pi R^2 + 2sR\right] \qquad (28)$$

Note that when ε=1, the ideal oval ducted fan, then $A_{DF} = \pi R^2 + 2sR$, as noted earlier.

Substituting the expression for the effective ducted fan exit area into the induced power ratio equation yields an expression for the ratio of oval duct-fan induced power to unducted (tandem) fan induced power. This expression includes the introduction of a duct efficiency factor, ε, $(0 \le \varepsilon \le 1)$. Ideal duct performance predicted when ε=1. When ε=0 the P_{DF}/P_{UDF} (induced power)=1 for all s/R values.

$$\left.\frac{P_{DF}}{P_{UDF}}\right|_{Induced\ Power} = \sqrt{\frac{2-m}{\left[(2-m)+(2+m)\varepsilon + \frac{4\varepsilon s}{\pi R}\right]}} \qquad (29)$$

Where m, the rotor overlap, is given by Eq. 26b and the duct efficiency, ε, is an empirical constant. Though the duct efficiency, ε, is treated as invariant with respect to s/R changes in the predictions in this paper, it probably does in actuality vary with s/R to some degree.